Imaging of Surface Acoustic Waves on GaAs Using 2D Confocal Raman Microscopy and Atomic Force Microscopy

Brian Douglas Rummel<sup>1</sup>, Leonid Miroshnik<sup>1</sup>, Marios Patriotis<sup>1</sup>, Andrew Li<sup>2</sup>, Talid R. Sinno<sup>2</sup>, Michael David Henry<sup>3</sup>, Ganesh Balakrishnan<sup>1</sup>, and Sang M. Han<sup>1,a)</sup>

<sup>1</sup>University of New Mexico, Albuquerque, New Mexico 87131, USA <sup>2</sup>University of Pennsylvania, Philadelphia, Pennsylvania 19104, USA <sup>3</sup>Sandia National Laboratories, Albuquerque, New Mexico 87185, USA

Surface acoustic wave devices have been fabricated on a GaAs(100) substrate to demonstrate the capability of 2D Raman microscopy as an imaging technique for acoustic waves on the surface of a piezoelectric substrate. Surface acoustic waves are generated using a two-port interdigitated transducer platform, which is modified to produce surface standing waves. We have derived an analytical model to relate Raman peak broadening to the near-surface strain field of the GaAs surface produced by the surface acoustic waves. Atomic force microscopy is used to confirm the presence of a standing acoustic wave, resolving a total vertical displacement of 3 nm at the antinode of the standing wave. Stress calculations are performed for both imaging techniques and are in good agreement, demonstrating the potential of this Raman analysis.

Surface Acoustic Waves (SAWs) are mechanical waves confined to the surface of a material, with an amplitude that decays exponentially toward the bulk of the substrate. SAWs are typically generated by interdigitated transducers (IDT) deposited onto a piezoelectric substrate. An IDT is constructed of an alternating finger pattern. The pitch of the finger pattern determines the wavelength of the acoustic wave. The SAW velocity is an inherent property of the substrate, and the resonant frequency is determined by the finger pitch and wave velocity. IDT devices are most commonly used in wireless network systems 1-6 and acousto-optic technologies<sup>7-11</sup>. These SAW-based devices have also found significant use as bio<sup>12</sup>, gas<sup>13,14</sup>, pressure<sup>15,16</sup>, and temperature 17,18 sensors as well as actuators, pumps, and mixers in microfluidic applications<sup>19,20</sup>. The purpose of this analysis is to improve our quantitative understanding of the surface stress induced by the SAWs. SAWs are often analyzed through electrical characterization, providing limited insight into the mechanical nature of surface acoustic wave devices. An improved understanding of mechanics and quantitative analysis would prove very useful in harnessing the benefits of stress-induced phenomena, such as compositional patterning in crystalline semiconductors<sup>21</sup>, increase in catalytic reaction rates<sup>22</sup>, and crystal growth applications<sup>23</sup>. We use 2D Raman analysis to directly measure the stress induced by SAWs and independently verify this approach with atomic force microscopy (AFM). The two techniques are used to fully characterize the stress and displacement imposed by SAWs.

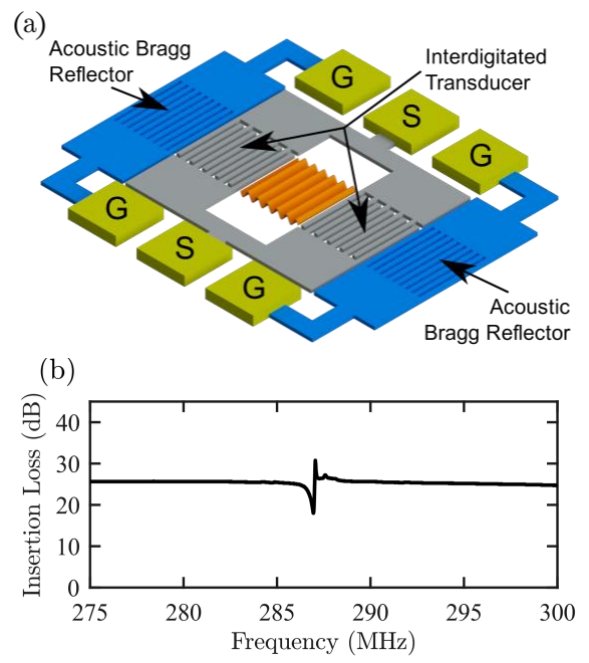


Figure 1: (a) IDT device modified to form a standing SAW. The alternating finger structure (grey) produces the SAW when the resonant rf potential is applied across the gold ground-signal-ground (GSG) pads. The standing SAWs (shown only as a conceptual drawing in orange) are observable in the center of the device. Acoustic Bragg Mirrors (blue) are included to contain the SAWs within the device, in a similar manner to a resonant cavity. (b) Insertion loss for the SAW IDT resonator used in this experiment. Insertion loss for the device-under-test achieves a minimum of 18.01 dB at the resonance frequency.

-

a) Author to whom correspondence should be addressed; Email: meister@unm.edu

Figure 1(a) provides a schematic diagram of the devices used in this work. The devices are fabricated on GaAs(100), positioned such that the waves propagate in the (110) direction. The device is based on a SAW resonator design; however, fingers are removed from the center of the device to provide a 200-µm-wide viewing window for the standing SAW strain field. Each side of the IDT is made up of 125 finger pairs and an acoustic Bragg reflector consisting of 100 grounded metal strips. The 100-nm-thick aluminum IDT structure is fabricated using optical lithography and electron-beam metal evaporation. A 10-nm-thick adhesion layer of titanium and a 1000-nm-thick gold layer are additionally deposited on top of the ground-source-ground (GSG) aluminum contact pads to form efficient electrical contact. The finger pitch of the IDT device (10 µm) determines the SAW wavelength,  $\lambda_{SAW} = v_{SAW}/f$ , where  $v_{SAW} = 2863\frac{m}{s}$  in the (110) direction for GaAs<sup>24</sup>. S-parameter and insertion loss measurements are performed using a Keysight 5247a RF Performance Network Analyzer. The resonance frequency is found to be 286.89 MHz, with the insertion loss reaching a minimum of 18.01 dB. This suggests that the device could be greatly improved, which would be possible by including more finger sets in the IDT. The device is wire-bonded to a quarter wavelength transmission line for impedance matching and is powered using a Windfreak Synth NV with a maximum applied power of 20.85 dBm.

The relationship between crystal strain and Raman peak shifts is widely established and well understood, especially for semiconductor systems<sup>25–27</sup>. Mechanical strain often affects the frequencies of the Raman modes in many crystal structures and follows a linear relationship between strain magnitude and Raman peak shift. Ganesan *et al.*<sup>28</sup> show that the frequencies of the three optical modes for diamond structures are linearly dependent on strain by solving the following secular equation:

$$\begin{vmatrix} p\varepsilon_{11} + q(\varepsilon_{22} + \varepsilon_{33}) - \lambda_0 & 2r\varepsilon_{12} \\ 2r\varepsilon_{12} & p\varepsilon_{22} + q(\varepsilon_{33} + \varepsilon_{11}) - \lambda_0 \\ 2r\varepsilon_{13} & 2r\varepsilon_{23} \\ 2r\varepsilon_{23} & \\ p\varepsilon_{33} + q(\varepsilon_{11} + \varepsilon_{22}) - \lambda_0 \end{vmatrix} = 0.$$

$$(1)$$

Here p, q, and r are material constants known as the phonon deformation potentials, and  $\varepsilon_{ij}$  are the individual components to the strain tensor. Bell  $et\ al.^{29}$  discuss how zinc-blende structures can be treated similarly, provided that the electrostatic forces induced by the piezoelectric nature of the crystal are sufficiently small. The secular equation refers to a crystallographic axis with  $\hat{x}_1 = [100]$ ,  $\hat{x}_2 = [010]$ ,  $\hat{x}_3 = [001]$ . In the case of a SAW traveling parallel to the  $\hat{x}' \parallel [110]$  direction, it is useful to apply a coordinate transformation on the secular equation, in which the strain field can be expressed (in the Voigt

notation) as  $\varepsilon = (\varepsilon'_{11}, 0, \varepsilon_{33}, 0, \varepsilon'_{13}, 0)$ .  $\varepsilon_{ij}$  are the strain components, and  $\hat{x}'_1 || [110], \hat{x}'_2 || [\bar{1}10]$ , and  $\hat{x}_3 || [001]$  define the axes of the transformed crystallographic orientation.

$$\begin{vmatrix} \frac{p}{2}\varepsilon'_{11} + \frac{q}{2}(\varepsilon'_{11} + 2\varepsilon_{33}) - \lambda_0 & r\varepsilon'_{11} \\ r\varepsilon'_{11} & \frac{p}{2}\varepsilon'_{11} + \frac{q}{2}(\varepsilon'_{11} + 2\varepsilon_{33}) - \lambda_0 \\ \sqrt{2}r\varepsilon'_{13} & \sqrt{2}r\varepsilon'_{13} \\ \sqrt{2}r\varepsilon'_{13} & \sqrt{2}r\varepsilon'_{13} \\ p\varepsilon_{33} + q\varepsilon'_{11} - \lambda_0 \end{vmatrix} = 0.$$
(2)

The strain components can then be described as a function of the transformed SAW stress field distribution:

$$\varepsilon'_{ij} = \begin{bmatrix} S_{11}\sigma'_{11} + S_{12}\sigma'_{22} + S_{12}\sigma_{33} \\ 0 \\ S_{12}\sigma'_{11} + S_{12}\sigma'_{22} + S_{11}\sigma_{33} \\ 0 \\ S_{44}\sigma'_{13} \\ 0 \end{bmatrix}.$$
(3)

Hooke's Law is used, applying a similar assumption made by Bell  $et\ al.^{29}$ . Additionally, the mechanical requirement for a surface wave is a stress-free surface, which can be stated as  $\sigma'_{i3}|_{x_3=0}=0$ . The penetration depth of the 532 nm laser into the GaAs substrate is ~1% of the wavelength of the SAW, so there will be very minimal contribution from the  $\sigma'_{i3}$  components to the Raman peak shift relative to the other non-zero components and are thus ignored. This makes the  $\varepsilon'_{13}$  component effectively zero, reducing the remaining two strain components to be functions of only  $\sigma'_{11}$  and  $\sigma'_{22}$ .

The change in Raman frequency for each mode in the presence of stress can be calculated from the eigenvalues:

$$\lambda_{0,j} = \omega_j^2 - \omega_{j,0}^2,$$
or
$$\Delta \omega_j = \omega_j - \omega_{j,0} \approx \frac{\lambda_{0,j}}{2\omega_{j,0}}.$$
(4)

 $\Delta\omega_j$  is the difference between the Raman frequency of each mode in the absence of stress,  $\omega_{j0}$  and in the presence of stress,  $\omega_j$ , The solutions to Eq. (2) yields three eigenmodes,  $\lambda_{0,j}$ , as well as their respective eigenvectors,  $\varphi_j$ . Two of the eigenmodes described by the 2×2 diagonal block in the upper region of Eq. (2) are associated with the transverse character and result from a mixing of the unperturbed transverse optical (TO) phonon modes<sup>30</sup>. The symmetry of the z-polarized mode is unmodified, and the Raman cross section of the longitudinal optical (LO) phonon mode remains equal to the case of the unperturbed crystal<sup>30</sup>. Additionally, the TO modes are not Raman

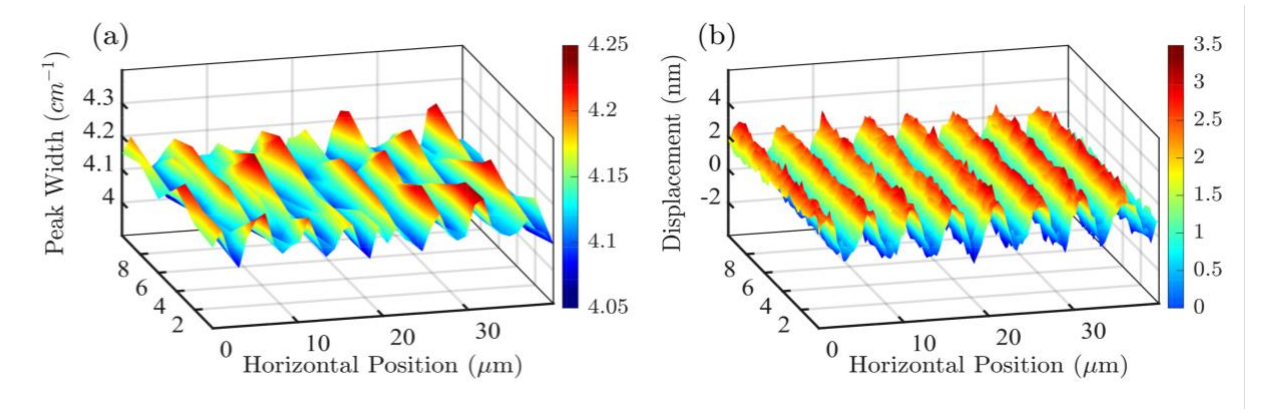


Figure 2: (a) 2D mapping of Raman peak widths of the LO phonon mode of GaAs associated with the standing wave structure of the SAW. (b) AFM topography analysis shows a precise depiction of the standing SAW.

active given the [001] backscattering geometry<sup>26,30</sup>, so only the LO frequency variations are considered for the variations in the Raman signal. The relationship between the crystalline stress induced by a surface acoustic wave and the frequency of the LO GaAs phonon mode is:

$$\Delta\omega_{LO} = \frac{1}{2\omega_0} [(pS_{12} + qS_{11})\sigma'_{11} + S_{12}(p+q)\sigma'_{22}], \quad (5)$$

where  $S_{ij}$  are the elastic compliance tensor elements of GaAs. The near-surface analysis of this technique allows  $\sigma'_{22}$  to be described as a linear combination of  $\sigma'_{11}$ . The mechanical boundary condition  $\varepsilon_{22} = 0 = S_{12}\sigma'_{11} + S_{11}\sigma'_{22}$  can be rearranged, and Equation (5) can be rewritten as:

$$\Delta\omega_3 = \frac{\sigma'_{11}}{2\omega_0} \left(\frac{S_{11} - S_{12}}{S_{11}}\right) \left(pS_{12} + q(S_{11} + S_{12})\right), \tag{6}$$

Using the values  $S_{11}=1.17\times 10^{-11}~{\rm Pa^{-1}}$  and  $S_{12}=-3.70\times 10^{-12}~{\rm Pa^{-1}}$  for the elastic compliance components<sup>31</sup> and  $p=-1.10\omega_0^2$ ,  $q=-1.58\omega_0^2$ , and  $r=0.51\omega_0^2$  for the phonon deformation potentials <sup>32</sup>, we find:

$$\Delta\omega_3(\text{cm}^{-1}) = -1.63 \times 10^{-9} \sigma'_{11}(\text{Pa})$$
 (7)

Under the presence of an acoustic wave, the surface of the crystal undergoes a rapid oscillation between compressive and tensile strain on the order of  $10^6$  to  $10^9$  oscillations per second, corresponding to the frequency of the acoustic waves. In order to determine the magnitude of strain induced by the SAW without using lock-in amplifier or interferometric techniques, it would be necessary to revisit the interpretation of Raman peak fitting. In this experiment, Raman peaks are fit using a Lorentzian function:

$$L = \frac{\left(\frac{c_0}{2}\right)^2}{\left((\omega - \omega_0)^2 + \left(\frac{c_0}{2}\right)^2\right)},\tag{8}$$

where  $c_0$  is the full width at half max (FWHM),  $\omega$  is the Raman shift position, and  $\omega_0$  is the peak position at its maximum. Iikawa et al. proposed that the Raman signature of a surface containing SAWs would result in a symmetrically broadened Raman peak at the anti-nodes of the standing wave due to the time averaging of the compressive and tensile states of the surface<sup>30</sup>. In this paper, we demonstrate this distinct peak broadening effect in the anti-node regions of the standing wave. Since the Raman peak shape can no longer be adequately fit with a Lorentzian function, it is ideal to use a time averaged Lorentzian in which the peak position is represented by the strain modulated peak position,  $\omega_0'(t) = \omega_0 +$  $\Delta\omega_0\sin(2\pi t/\tau_{SAW})$ , where  $\Delta\omega_0$  is the maximum peak shift achieved by the standing SAW for any given point in time and  $\tau_{SAW}$  is the temporal period of the SAW. The time averaged integral reveals:

$$F = \frac{A}{2\Delta\omega_0} \left[ \tan^{-1} \left( \frac{\Delta\omega_0 + (\omega - \omega_0)}{c_0/2} \right) + \tan^{-1} \left( \frac{\Delta\omega_0 - (\omega - \omega_0)}{c_0/2} \right) \right], \tag{9}$$

where the proportionality factor, A, has been introduced to account for the amplitude of the Raman peak and can be ignored after normalization of the Raman data.

The 2D Raman spectra, shown in Fig. 3, are gathered using a WITec Confocal-Raman 532 nm Microscope. The laser light is focused to an 850 nm spot size using a  $50\times$  objective. The laser power used for this experiment is approximately 1 mW. In order to produce the Raman image, eight equally spaced, 40  $\mu$ m line scans are recorded and stitched together. The acquisition time for each point of the line scan is 15 seconds, and the point

acquisition is repeated three times to reduce the noise. The spacing between adjacent points is 1  $\mu$ m. The mapping data are recorded over a  $10\times40~\mu\text{m}^2$  area, for a total of 329 points, in the center of the viewing window region of the device. The total acquisition time is approximately 4 hours. Stress analysis is completed by examining the 291.7 cm<sup>-1</sup> LO phonon Raman peak. First, scans are recorded while the device is turned off, where the Raman data show homogeneous behavior. The device is then turned on and tuned to the resonant frequency to activate the SAW field, and the same image scan procedure is completed.

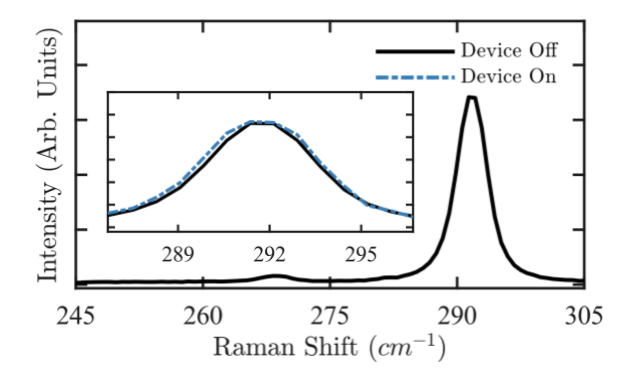
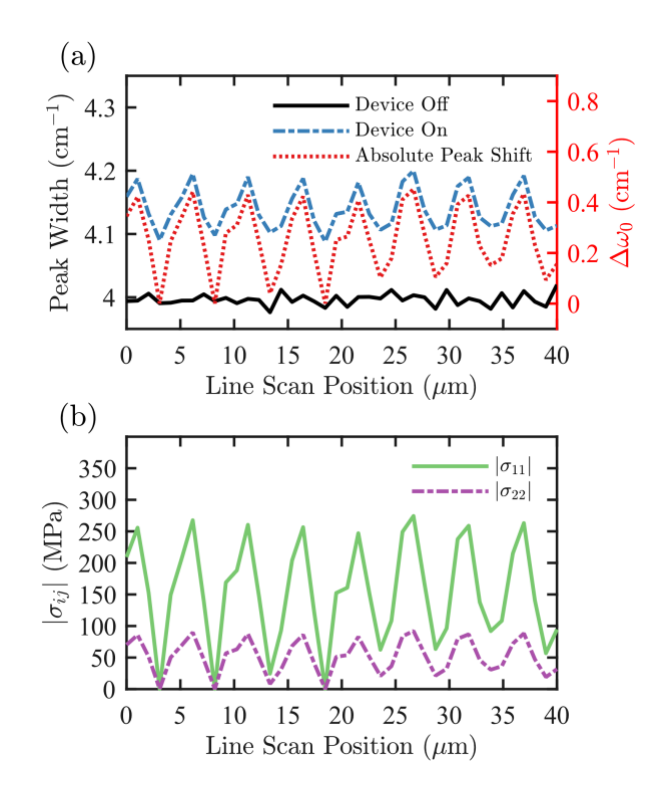


Figure 3: Raman spectra of GaAs showing the TO peak at 268.3 cm<sup>-1</sup> and the LO peak at 291.7 cm<sup>-1</sup>. The inset depicts the widening of the LO Raman peak (blue) when measured from the antinode region of the standing SAW.

Figure 2(a) depicts the apparent peak widths of the GaAs LO phonon Raman peak. The broadening of the Raman peak is observed at intervals of 5 µm, implying an acoustic wavelength of 10 µm, as expected, and the apparent width increases to values as high as 4.25 cm<sup>-1</sup> in the anti-nodal regions of the standing SAW. The Raman peak width image is averaged into a single line scan, shown in Fig. 4(a). While the device is off, the peak width is observed to be around 4.00 cm<sup>-1</sup> at a peak position of 291.76 cm<sup>-1</sup>. When the device is turned on, peak widths, on average, oscillate between 4.09 cm<sup>-1</sup> and 4.20 cm<sup>-1</sup> at a relatively stagnant peak position of 291.69 cm<sup>-1</sup>. One might expect the Raman peak to show no broadening in the nodal regions of the standing wave; however, there is instead a 0.09 cm<sup>-1</sup> increase. There are a few reasons why this homogenous broadening of the Raman peaks would occur: (1) heating of the GaAs substrate from the IDT device<sup>33</sup>, (2) the spatial average of the strain field due to the relatively large lateral resolution of the Raman laser, and/or (3) the coupling of the phonon wave vectors induced by the nonhomogeneous distribution of the SAW fields<sup>30</sup>. This constant peak broadening effect would make analysis of a traveling SAW field difficult, so additional studies should be completed to determine the cause of this effect.



**Figure 4:** (a) Raman peak widths while the device is turned off (black) and while the device is turned on (blue). The resulting fitted peak shifts are shown on the right axis (red). (b) Eq. 7 allows for the calculation of  $|\sigma'_{11}|$  and  $|\sigma'_{22}|$ .

After fitting the Raman curves with the new fitting procedure defined by Eq. (9), we discover that, in the antinodal regions of the SAW, the Raman peak shifts as much as 0.42 cm<sup>-1</sup> to the left and right, during the tensile and compressive states of the SAW, respectively. As shown in Fig. 4(b), this translates to maximum  $|\sigma'_{11}|$  and  $|\sigma'_{22}|$  values of 260 MPa and 87 MPa. Applying these values to Eq. (3) provides strain values of  $2.9 \times 10^{-3}$  and  $1.4 \times 10^{-3}$  for  $|\varepsilon'_{11}|$  and  $|\varepsilon'_{33}|$ , respectively.

Contact-mode atomic force microscopy is employed to confirm the magnitude of surface displacement caused by the standing SAWs. The dynamic nature of the acoustic strain field restricts the AFM cantilever to profile only the absolute displacement of the standing SAW. Contact-mode analysis may impart an impression that the AFM cantilever would attempt to track the motion of the acoustic wave and thus provide an inaccurate, timeaveraged measurement. This is not the case, however, as the vibrational frequency of the silicon cantilever used in this experiment is on the order of 105 Hz, while the frequency of the SAW is on the order of 108 Hz. The response time of the cantilever is too slow to track the acoustic wave and is able to measure the maximum positive excursion of SAWs. The 2D imaging results of the AFM profile of the standing SAW field are shown in Fig. 2(b).

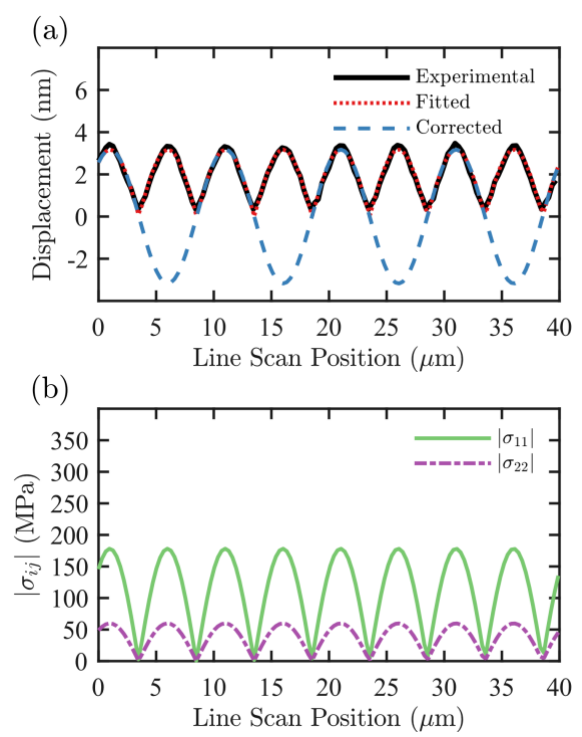


**Figure 5:** (a) The fitted curve (red) for the absolute vertical displacement (black) induced by the standing SAW shows a maximum displacement of 3 nm and a wavelength of  $10 \mu m$ . The corrected curve (blue) represents the true shape of the standing SAW. (b) The values for the fitted data to displacement allows for the calculation of  $|\sigma'_{11}|$  and  $|\sigma'_{22}|$ .

Figure 5(a) shows the vertical line average of the 2D AFM image and the corresponding fitted and corrected profile. We assume that the vertical displacement induced by the SAW wave could be fit with an absolute sine function, which is in agreement with the analytical solution for a SAW<sup>24</sup>. Figure 5(a) depicts the results of this analysis. The red curve shows the fitting results for the absolute sine function and predicts a SAW wavelength of 10 µm and an amplitude of 3 nm. Combining the fitted data with the mechanical boundary conditions for a SAW as well as Hooke's Law, the stress values induced by the SAW are calculated and shown in Fig. 5(b). The AFM analysis predicts  $|\sigma'_{11}|$  and  $|\sigma'_{22}|$  values of 178 MPa and 60 MPa, respectively, in the anti-nodal regions of the standing SAW. For a more precise comparison, it would be ideal to measure the displacement induced by the standing SAW using interferometry techniques and acquire Raman data using a higher resolution spectrometer, which is outside of the scope of this paper.

In conclusion, the relationship between the Raman peak broadening and the crystal strain induced by the standing surface acoustic waves is defined, and stress values are acquired using a unique Raman peak fitting scheme. These stress values agree well with the data collected from the AFM, thus demonstrating the potential of 2D Raman microscopy for the characterization of SAW fields and devices. Future studies will address the potential effects of substrate heating from the device and will acquire more accurate surface displacement data.

## Acknowledgments

Funding for this research was provided by the National Science Foundation under award number DMR-1809095.

## **Data Availability**

The data that support the findings of this study are available from the corresponding author upon reasonable request.

## References

<sup>1</sup> C. Campbell, Surface Acoustic Wave Devices and Their Signal Processing Applications (1989).

<sup>2</sup> C.C.W. Ruppel, L. Reindl, and R. Weigel, IEEE Microw. Mag. **3**, 65 (2002).

<sup>3</sup> C.C.W. Ruppel, IEEE Trans. Ultrason. Ferroelectr. Freq. Control **64**, 1390 (2017).

<sup>4</sup> L.M. Reindl, A. Pohl, G. Scholl, and R. Weigel, IEEE Sens. J. 1, 69 (2001).

F. Seifert and R. Weigel, 1997 27th Eur. Microw. Conf. EuMC 1997
 1323 (1997).

<sup>6</sup> T. Morita, Y. Watanabe, M. Tanaka, and Y. Nakazawa, in *Proc. - IEEE Ultrason. Symp.* (1992), pp. 95–104.

<sup>7</sup> C.J. Sarabalis, T.P. McKenna, R.N. Patel, R. Van Laer, and A.H. Safavi-Naeini, APL Photonics **5**, (2020).

<sup>8</sup> P.J.M. van der Slot, M.A.G. Porcel, and K.-J. Boller, Opt. Express **27**, 1433 (2019).

<sup>9</sup> S. Kakio, Acta Phys. Pol. A 127, 15 (2015).

<sup>10</sup> M. van der Poel, M. Beck, M.B. Duhring, M.M. de Lima, L.H. Frandsen, C. Peucheret, O. Sigmund, U. Jahn, J.M. Hvam, and P. Santos, Proc. ECIO 07 3 (2007).

<sup>11</sup> M.M. De Lima and P. V. Santos, Reports Prog. Phys. **68**, 1639 (2005).

<sup>12</sup> M.R. Zakaria, M.A.F. Shamsuddin, U. Hashim, T. Adam, and A.W. Al-Mufti, in *Proc. - Int. Conf. Intell. Syst. Model. Simulation, ISMS* 

- (2015), pp. 760-764.
- <sup>13</sup> J. Devkota, P.R. Ohodnicki, and D.W. Greve, Sensors (Switzerland) 17, 13 (2017).
- <sup>14</sup> E. Benes, M. Groschl, W. Burger, and M. Schmid, Sensors Actuators A 1, (1995).
- <sup>15</sup> P. Nicolay, H. Chambon, G. Bruckner, C. Gruber, S. Ballandras, E. Courjon, and M. Stadler, Sensors (Switzerland) 18, (2018).
- <sup>16</sup> T. Hoang, Design and Realization of SAW Pressure Sensor Using Aluminum Nitride, L'Universite Joseph Fourier, 2009.
- <sup>17</sup> C. Fu, Y. Ke, M. Li, J. Luo, H. Li, G. Liang, and P. Fan, Sensors (Switzerland) 17, (2017).
- <sup>18</sup> L.M. Reindl and I.M. Shrena, IEEE Trans. Ultrason. Ferroelectr. Freq. Control **51**, 1457 (2004).
- <sup>19</sup> X.Y. Du, Y.Q. Fu, J.K. Luo, A.J. Flewitt, and W.I. Milne, J. Appl. Phys. **105**, (2009).
- <sup>20</sup> C.D. Wood, S.D. Evans, J.E. Cunningham, R. O'Rorke, C. Wälti, and A.G. Davies, Appl. Phys. Lett. 92, 20 (2008).
- <sup>21</sup> D. Kaiser, S.M. Han, and T. Sinno, J. Appl. Phys. **121**, (2017).
- <sup>22</sup> B. von Boehn, M. Foerster, M. von Boehn, J. Prat, F. Macià, B.

- Casals, M.W. Khaliq, A. Hernández-Mínguez, L. Aballe, and R. Imbihl, Angew. Chemie Int. Ed. (2020).
- <sup>23</sup> M.J. Aziz, P.C. Sabin, and G.Q. Lu, Phys. Rev. B 44, 9812 (1991).
- <sup>24</sup> R. Mathew, Creating and Imaging Surface Acoustic Waves on GaAs, 2009.
- <sup>25</sup> P. Taylor and R. Loudon, Advances in Physics The Raman Effect in Crystals (2010).
- <sup>26</sup> I. De Wolf, Semicond. Sci. Technol. **11**, 139 (1996).
- <sup>27</sup> E. Pittarello, Phys. Rev. B **5**, 580 (1972).
- <sup>28</sup> S. Ganesan, A. Maradudin, and J. Oitmaa, Ann. Phys. (N. Y). **594**, 556 (1970).
- <sup>29</sup> M.I. Bell, Phys. Stat. Sol. **53**, 675 (1972).
- <sup>30</sup> F. Iikawa, A. Hernández-Mínguez, M. Ramsteiner, and P. V. Santos, Phys. Rev. B 93, 1 (2016).
- <sup>31</sup> S. Adachi, J. Appl. Phys. **58**, R1 (1985).
- <sup>32</sup> M. Hunermann, W. Richter, and J. Saalmuller, Phys. Rev. B **34**, 5381 (1986).
- <sup>33</sup> A.M. Ardila, O. Martínez, M. Avella, J. Jiménez, B. Gérard, J. Napierala, and E. Gil-Lafon, J. Appl. Phys. 91, 5045 (2002).